Journal of Thermal Science and Engineering Applications,
Volume 13, Issue 4, August 2021, Article number 041010; Paper number TSEA-20-1428
DOI:10.1115/1.4048757

Numerical investigation on turbulence statistics and heat transfer of a circular jet impinging on a roughened flat plate

Abdulrahman Alenezi, first author[1]
Department of Mechanical Power and Refrigeration, College of Technological studies, Shuwaikh, Kuwait
E-mail: ah.alenezi@paaet.edu.kw
000102754950

Abdulrahman Almutairi, second author
Department of Mechanical Power and Refrigeration, College of Technological studies, Shuwaikh, Kuwait
E-mail: asa.almutairi@paaet.edu.kw

Hamad Alhajeri, third author
Department of Mechanical Power and Refrigeration, College of Technological studies, Shuwaikh, Kuwait
E-mail: hm.alhajeri@paaet.edu.kw

Abdelaziz Gamil, fourth author
Department of Power and Propulsion, Cranfield, Cranfield University, UK
E-mail: a.gamil@cranfield.ac.uk

Faisal Alshammari, fifth author
Ministry of Electricity and Water, Shuwaikh, Kuwait
Email: Eng_faisal_1@hotmail.com

[1] Corresponding author: Abdulrahman Alenezi, Department of Mechanical Power and Refrigeration, College of Technological studies, Shuwaikh, Kuwait. Email: Ah.alenezi@paaet.edu.kw

ABSTRACT

A detailed heat transfer numerical study of a three-dimensional impinging jet on a roughened isothermal surface is presented and is investigated from flow physics vantage point under the influence of different parameters. The effects of the Reynolds number, roughness location, and roughness dimension on the flow physics and heat transfer parameters are studied. Additionally, the relations between average heat transfer coefficient and flow physics including pressure, wall shear and flow vortices with thermodynamic non-equilibrium are offered. This paper studies the effect of varying both location and dimension of the roughness element which took the shape of square cross-section continuous ribs to deliver a favorable trade-off between total pressure loss and heat transfer rate. The roughness element was tested for three different radial locations (R/D) =1, 1.5 and 2 and at each location its height (i.e. width) (e) was changed from 0.25 to 1 mm in incremental steps of 0.25. The study employed a jet angle (α) of 90°, jet-to-target distance (H/D=6) and Re ranges from 10,000 to 50,000, where H is the vertical distance between the target plate and jet exit.

The results show that the average heat transfer coefficient (AHTC) can be significantly affected by changing the geometry and dimensions of the roughness element. This variation can be either an augmentation of, or decrease in, the (HTC) when compared to the baseline case. An enhancement of 12.9 % in the AHTC was achieved by using optimal location and dimensions of the roughness element at specific Reynolds number. However, a diminution between 10% to 30% in (AHTC) was attained by the use of rib height e=1mm at Re=50K. The variation of both rib location and height showed better contribution in increasing heat transfer for low-range Reynolds numbers.

1. INTRODUCTION

In the aerospace industry, increasing the temperature of the working fluid is a well-known condition when seeking to improve machinery efficiency. However, this condition is restricted by the melting points of metals. An alternative technique is to increase heat transfer rate where it is needed, e.g. the use of turbulators in jet impingement. The latter method has been the focus of recent research into improving heat transfer using roughening elements, which can improve the heat transfer rate by both enlarging the surface area and increasing flow turbulence, depending on type and size Sasmito et al. [1]. Increased the roughness of the heated surface rises heat transfer by disturbing the thermal sublayer in the

stagnation region Gabour & Lienhard [2]. However, it can also change the flow physics by causing a pressure loss which decreases heat transfer rate [3, 4]. Previous studies [5, 6] have reported an increase of approximately 50% to 60% in heat transfer rate when using roughness elements compared to the case of a smooth surface.

The main disadvantages of using roughness elements are enlarged surface area, increasing equipment weight and generating thermal stresses, especially for roughness elements with sharp edges [7, 8]. The latter could cause thermal failure, but the likelihood can be reduced by using roughness elements with round edges. Kim & Lee [9] performed a series of experiments on fluid flow and heat transfer characteristics of a heated porous surface composed of various sizes of glass beads subject to the impingement of water droplets. They constructed four porous surfaces with different levels of surface roughness and permeabilities. They defined the existence of two primary impingement areas; contact and non-contact: the non-contact area is where the water droplets appeared suspended in the air, above the hot surface, due to surface film boiling; the contact area was where the water droplets boiled/evaporated on contact with the hot surface. Celik [10] used a co-axial jet in the form of two concentric pipes to compare heat transfer from a smooth and then artificially roughened heated surface subjected to co-axial jet impingement. He confirmed that a rough surface gave better heat transfer and ascribed this to disruption of the boundary layer. He also found that the co-axial jet improved heat transfer above that for a single circular jet by as much as 27%. Xing & Weigand [11] carried out an experimental investigation of jet impingement and heat transfer subject to different cross-flows for both dimpled and smooth surfaces. They found that a jet/plate separation of three times the jet diameter (H/D=3) consistently gave maximum heat transfer. They also found that a dimpled surface enhanced the maximum heat transfer rate above that of the smooth plate by up to 12%.

An investigation of the thermal performance of a solar air heater with changes in the height/width ratio of V-shaped roughening elements in a staggered arrangement, for Reynolds numbers in the range 5,000 to 19,000 reported that maximum overall thermal performance was for Reynolds number of 16,000 and relative width ratio of 6.0 Nadda et al. [12]. Wang et al. [13] employed a dimpled wall in a converging channel in a numerical investigation. A bleed hole was added to the dimple to form a cavity with insulation angles ranging between −30° to 30°. Recent research by Lo and Liu has introduced original parameters to describe the effect of jet impingement on heat transfer (local and average Nusselt numbers) for smooth and roughened surfaces. These included Richardson number, solid volume fraction, and roughness element orientation. The heated surface was roughened using rectangular grooves allied with the jet holes arranged either parallel or orthogonal to the exit flow. The authors reported an enhancement of about 50% in heat transfer for longitudinal grooves with a noticeable improvement observed near the groove edges. Alhajeri et al. [14] investigated numerically the effect of roughening elements inside vortex chamber on heat transfer rate and flow physics. Flow physics parameters included in their study were, total pressure loss, thermal performance factor, Nusselt number and entropy generation. In another study, Attala et al. [15] investigated the effect of protrusion size on local and average Nusselt number. The protrusion which had a cubic shape with 400 μm × 400 μm square cross-section and depths that varied from 100 to 300 μm improved the average Nu by between 10 to 32%. Wang et al. [16] investigated the effect of using bidirectional ribs in a microchannel heat sink on the thermo-hydraulic performance experimentally. They reported that the heat transfer rate could be noticeably increased by using bidirectional ribs as a result of interrupting the thermal boundary layer and inducing vortices in both spanwise and vertical directions. The roughened heat sink has been of interest in numerous experimental and

numerical studies aiming to discover novel hydrothermal aspects, especially of the pin-fin roughening type. Such aspects will depend on multiple factors such as pin-fin morphology, tip clearance and porosity [17, 18]. Kewalramani et al. [19] employed a pin-fin heat sink in their numerical investigation to study thermal and hydraulic performance and reported new correlations of Nusselt number and Poiseuille number. Choudhary et al. [20] used wings in their experimental investigation to enhance the heat transfer rate of a pin fin heat sink when compared to a heat sink without wings for both inline and staggered arrangements. Ratios of wing size and fin pitch were the focus of this study. Newly et al. [21] investigates the effect of employing different shapes of micro-pin fin in heat sink on overall heat transfer and pressure drop characteristics. Their numerical study used hydrofoil and sine shaped pin-fins. The latter shape showed the lowest pressure loss and best heat removal capacity at 100 ml/min coolant flow rate.

Wang et al. [22] studied the impact of using different arrangements of inlet and outlet locations on the performance of a heat sink roughened by the addition of pin-fins.

Wang et al. [23] studied numerically the effect of employing truncated ribs (TRs) on the sidewalls of a microchannel heat sink on flow and heat transfer characteristics. The authors investigated the effect of varying TR height, rib geometry including height and width on the hydrothermal performance reporting that an obvious enhancement can be reached by using TRs especially at the truncation gap where large decrease of pressure loss occurs.

Several micro-roughness shapes were investigated by Singh et al. in their numerical and experimental study of jet impingement. They reported that an enhancement in a heat transfer rate of between 20% to 60% could be reached by roughening the heated wall. Ravanji & Zargarabadi [24] discovered that the heat transfer rate between the heated pinned surface and the jet increases due to the turbulence region that exists around the pins. This finding has

also been reported by Hadipour et al. [25], who also found that the concave surface of the pins has a lower minimum temperature compared to a smooth concave surface.

Several types and shapes of protrusions on the target surface have been reported in the literature with either fixed dimensions or locations or both. However, no attempts were found in the literature to evaluate the impact of varying both dimension and location of the roughness element on impingement cooling performance. This paper should help cover this gap in the literature.

In this research, the effect of using a roughness element in the shape of a circle with square cross section, and with the same center as the jet (Figure1) on the average heat transfer coefficient will be investigated. The effectiveness of the roughness element will be tested for three different radii (R) and four heights (e). The research paper is divided into two main sections:

The effect of Turbulator Location and turbulator dimension on both flow physics and heat transfer characteristics. The rib will be tested for three different locations, R= 1D, 1.5D and 2D where D is the jet hydraulic diameter, and for each location it will be tested for four different rib heights (e) between 0.25 mm and 1.5 mm in increments of 0.25 mm to ascertain the optimum height for each location. This range of rib locations should extend from within to outside the stag-nation region. Figure 1 shows the geometry of the uniform circular rib. The total number of simulated cases is 65.

2. COMPUTATIONAL SETUP AND NUMERICAL SCHEME

Fig. 1 shows the computational domain, mesh details and boundary conditions for the intended problem. Due to the axisymmetric nature of flow and geometry, only half of the domain was simulated to save computational time. To validate the current study, all dimension details have been extracted from the experimental work of O'Donovan & Murray

[26] and the numerical study of Alimohammadi et al. [27] and normalized to the jet hydraulic diameter (D). The domain which has a circular shape has a diameter of 40D and includes the isothermal wall. The jet which has a fully developed profile was pre-simulated separately and imposed at the jet inflow. A very fine mesh was used on the whole domain, especially in the stagnation region and the rib, in order to accurately capture the heat transfer rate. The y+ value near the wall was kept below 1 as recommended in the literature for this type of jet impingement. The fluid used in this application is air at room temperature leaving an unconfined jet with hydraulic diameter (D) of 13.5 mm to impinge on an isothermal flat surface maintained at 60 °C. The wall has a no-slip condition and was located at H/D=6 below the jet. The top and side surfaces were set to be pressure outlets maintained at ambient temperature. Reynolds numbers were changed from 10,000 to 50,000 in steps of 10,000, where all air properties were taken for 1 atm and room temperature. Finally, The numerical results were successfully validated against the experimental data of O'Donovan and Murray [26] and the numerical study of Alimohammadi et al. [27] which were for a smooth surface (no rib) and will be treated as the baseline case in all later calculations. The effect of using a roughness element in the shape of a circle with square cross section, and with the same center as the jet on the average heat transfer coefficient will be investigated. The effectiveness of the roughness element will be tested for three different radii (R) , R= 1D, 1.5D, 2D and four heights (e) between 0.25 mm and 1.5 mm in increments of 0.25 mm to ascertain the optimum height for each location. This range of rib locations should extend from within to outside the stagnation region.

Governing Equations

The three-dimensional steady-state incompressible Reynolds Average Navier–Stokes (RANS)

$$\frac{\partial U}{\partial Z}+\frac{\partial U}{\partial r}+\frac{V}{r}$$

$$= 0 \quad (1)$$

$$\rho\left(U\frac{\partial U}{\partial Z}+V\frac{\partial U}{\partial r}\right)=-\frac{\partial P}{\partial Z}+\frac{1}{r}\frac{\partial}{\partial r}\left[r\left(\mu\frac{\partial U}{\partial r}-\rho\overline{u'v'}\right)\right]+\frac{\partial}{\partial z}\left[\left(\mu\frac{\partial U}{\partial z}-\rho\overline{u\cdot u'}\right)\right] \quad (2)$$

$$\rho\left(U\frac{\partial V}{\partial Z}+V\frac{\partial V}{\partial r}\right)=-\frac{\partial P}{\partial r}+\frac{1}{r}\frac{\partial}{\partial r}\left[r\left(\mu\frac{\partial V}{\partial r}-\rho\overline{v'v'}\right)\right]+\frac{\partial}{\partial z}\left[\left(\mu\frac{\partial U}{\partial z}-\rho\overline{u\cdot u'}\right)\right]-\mu\frac{V}{r^2} \quad (3)$$

$$\rho C_p\left(U\frac{\partial T}{\partial Z}+V\frac{\partial T}{\partial r}\right)=\lambda\left[\frac{\partial}{\partial r}\left(\frac{\partial T}{\partial r}\right)+\frac{1}{r}\frac{\partial T}{\partial r}+\frac{\partial}{\partial z}\left(\frac{\partial T}{\partial z}\right)\right]+\overline{\Phi}-\rho C_p\left(\frac{\partial\overline{u't'}}{\partial z}+\frac{\partial\overline{v't'}}{\partial r}-\frac{\partial\overline{v't'}}{r}\right) \quad (4)$$

Where $\overline{\Phi}$ is the viscous dissipation heat source

$$\overline{\Phi}=2\,\mu\left[\left(\frac{\partial V}{\partial r}\right)^2+\left(\frac{V}{r}\right)^2+\left(\frac{\partial U}{\partial z}\right)^2+\frac{1}{2}\left(\frac{\partial V}{\partial z}+\frac{\partial u}{\partial z}\right)^2\right] \quad (5)$$

Solution Method and Validation

An axisymmetric numerical simulation was performed using Ansys v 18 [28]. To accurately simulate the results, the spatial discretization employed in this investigation was the SIMPLEC scheme and Green-Gauss cell-based gradient, using the second-order for both energy and momentum equations. The solution was initialized using the standard initialization by inlet conditions with convergence criteria of 10^{-6} for energy and continuity equations, and10^{-4} for the other equations.

Fig. 2 (a), presents a comparison between simulated results data of local Nusselt number for different grid meshes with the experimentally determined values as a function of radial distance (R/D), for H/D=6 and jet angle 90° as used by O'Donovan & Murray [26]. Fig. 2 (b) presents the simulated local Nusselt number results for different turbulence models in comparison with the same experimental data and numerical data of Alimohammadi et al. [27] . It is seen that the results did not vary significantly with mesh size. Thus, for convenience and ease of calculation, the 400k mesh was used for all remaining calculations and simulations. Test runs were undertaken using the RMS, RNG k-epsilon (k-ε), and SST k-omega turbulence

models to assess how well they predicted the value of the local Nusselt number as a function of R/D for H/D=6 and jet angle 90°. When the results were compared, overall, the RNG k-epsilon model produced the best agreement with the experimentally determined local Nu values. In particular, it accurately (error of less than 2%) predicted the value of Nu at the stagnation point. Both the RMS and SST k- ω models overestimated Nu at the stagnation point by 21% and 18 % respectively. However, no model produced the small trough seen in the experimental plot at R/D ≈2. Based on this evaluation, the RNG k-epsilon model was selected for this parametric study. The average Nusselt number over the average area $0 \leq R/D \leq 3.5$ obtained from the current simulation is validated and compared to the experimental study of Sagot et al. [30] and showed in Fig.2 (c) . The figure shows good agreement between experimental and numerical data for $10{,}000 \leq Re \leq 30{,}000$, R/D=3.5 and H/D =6 with maximum percentage error of 2.9% at Re=30,000.

3. RESULTS AND DISCUSSION

3.1. Smooth Wall Flow Physics and Heat Transfer Characteristic - The Baseline Case

Local static pressure distributions as functions of Reynolds number, for jet flow impinging on a flat plate, (H/D = 6, α = 90°) are shown in Fig. 3. Generally, regardless of flow Reynolds number, the maximum static pressure is always detected at the stagnation point at the expense of velocity on the flat surface, followed by a noticeable almost linear degradation until radial distance y/D=1.5. In the downstream direction where y/D ≥1.5, static pressure *is independent of Reynolds numbers* and constantly remains stable at a value of approximately zero with the slight pressure gradient along radial direction. The figure shows that static

pressure is highly sensitive to Reynolds number values in the range of 0 ≤y/D ≤1.5. Briefly, the higher Reynolds number the higher pressure at stagnation point. Furthermore, Gradient of pressure along radial direction (∂ P / ∂ r) is increases with Reynolds number for a radial span of 0 ≤r / d ≤1. Pressure distribution does not depend on Reynolds number at downstream radial locations (r / d ≥1). The study made by Baghel et.al [29] reported same static pressure trend with more details for such observation.

Fig. 4 shows local wall shear stress distribution in the downstream direction for different Reynolds numbers. The same curve trend is seen for all Re, starting from zero shear stress at the stagnation point then increasing rapidly to reach a peak value. However, as Re increases, this peak value which corresponds to the maximum pressure gradient (∂P/∂y) moves slightly downstream, in the direction of y increasing. Past this point, the curve starts to decrease rapidly until y/D≈2, after which there is a more gradual decrease in shear stress that continues until it reaches almost a constant value at radial distances y/D ≥ 9 due to the negligible pressure gradient observed earlier in Fig. 3 at y/D≥ =1.5.

Heat transfer characteristics of a heated plate in the case of fixed two reference temperatures, subjected to free surface jet impingement is quantified using a local heat transfer coefficient, which is calculated as:

$$h = \frac{\varphi}{T_w - T_j} \qquad (6)$$

Where $\boldsymbol{\varphi}$ is the convective wall flux density, $T_w \; and \; T_j$ represent the wall and jet temperature respectively.

The corresponding local Nusselt number can be determined by:

$$\mathrm{N_u} = {}^{\mathrm{hD}}/_{\mathrm{k}} \qquad (7)$$

With D the jet hydraulic diameter and k is the gas thermal conductivity

The mean or average heat transfer coefficient of a circular plate of radius R is obtained by

$$\bar{h}\,(R) = \frac{1}{\pi R^2}\,\frac{\Phi(R)}{T_w - T_j} \qquad (8)$$

Where $\boldsymbol{\Phi}(R)$ is the heat flux which can be averaged over a circular plate using:

$$\Phi(R) = \int_0^R \Phi(r) 2\,\pi r dr \qquad (9)$$

Fig. 5 shows a linear variation of average heat transfer coefficient (of $\overline{h_o}$) of the baseline case with varying Reynolds number. These values of $\overline{h_o}$ were averaged between 0 ≤ R/D ≤ 2.5 to capture the effect of varying Re on heat transfer. The average heat transfer coefficient varies linearly with and Reynolds number. Changing Reynolds number from 10,000 to 50,000 increased the average heat transfer coefficient by approximately 303%, indicating the major impact of flow velocity on heat transfer characteristics.

3.2. Roughened Wall

Effect of Turbulator Location - Flow Physics

Fig. shows the effect of varying rib location and Reynolds numbers on the size and shape of flow vortices before and after the rib. Rib height is e=0.5 mm and its location was changed from R/D=1 to R/D=2 for Reynolds number 10k,30k and 50k. In general, the figure indicates that a flow separation happens in front of the rib resulting in a small separation region followed by a larger after-rib recirculation vortex. The figure also shows that as both Reynolds number and rib radial location increases so does the length of the vortices. It is worth saying that the shape and length of these vortices could noticeably affect the local heat transfer rate. In addition, flow recirculation can be seen above the roughness element and this could

prevent the incoming jet from re-attaching to the heated surface, as shown in the particular case of Re=50k, R/D=2 and e=1mm where the main jet failed to reattach.

Fig 7 illustrates local static pressure distribution over a flat plate for selected Reynolds numbers. Generally, the local pressure at the stagnation point won't be substantially affected regardless of the rib location for lower and intermediate Reynolds numbers. The major effect of the roughness element takes place just before and after the flow meets the rib regardless of its location. For all three rib locations, a noticeable local pressure peak occurs just before the rib due to the impact between the flow and the rib, where the flow velocity is reduced because of this impact. The pressure peak value is less for lower Reynolds numbers and for the rib located further downstream. Furthermore, after the flow passes the rib, a low-pressure zone, usually called the "wake" is seen downstream of the rib, commencing immediately behind the rib due to differences in the flow pressure magnitudes resulting in negative static pressure as shown in the figure.

To continue examining the effect of rib location on flow kinematics, Fig. compares wall shear stress distribution for the no rib case and with the rib of height 0.50 mm, Reynolds numbers were 10k,30k and 50k for each of three rib locations. The rib effect takes place just when the flow reaches the rib causing the first local minima due the effect of the small flow recirculation zone on the pressure gradient ($\partial P/\partial y$). When the jet hits the rib, a wall shear peak occurs and it separates from the wall forming a low pressure region where a larger flow recirculation zone occurs which effects the main flow velocity, creating a local maximum and second local minimum value of shear stress. The contour shown in the figure displays a maximum wall shear peak location on the rib. The peak value of wall shear stress at R/D=1 is approximately 40% bigger than its value at R/D=2.

Effect of Turbulator Location - Heat Transfer Characteristic

To demonstrate how change in rib location and Reynolds number effect heat transfer rate, Fig. shows the local heat transfer coefficient for different rib locations and different Reynolds numbers, and compares them to the baseline case. The figure shows that for all three locations of the rib, the local heat transfer curve for the no rib case showed higher local values in front of the rib than when the rib was present. The stagnation heat transfer coefficient value for the no rib case for Reynolds number 50k is about 20% more than its value when a rib is present regardless of rib location. The local heat transfer coefficient curve shows an obvious peak as a result heat exchange between the main flow and the heated rib due to the existence of vortices in front of it resulting in higher turbulence intensity. As shown in the figure, the local value of this peak depends on rib location and decreases as the rib location moves downstream. In the specific case of Re=30k, for example, the local heat transfer coefficient peak values were 2232, 2089 and 1965 W/(m^2.K) for R/D=1, 1.5 and 2, respectively.

Fig. presents the average heat transfer coefficient normalized to the baseline value ($\overline{\mathrm{h_o}}$). Clearly for the case of e=0.50 mm, the most effective location for the rib is at R/D = 2, for which ($\bar{\mathrm{h}}/\overline{\mathrm{h_o}}$) gives higher percentage increase for all Reynold numbers when compared to other rib locations. The percentage increase of average heat transfer coefficient for R/D=1 is between 0.2% and 6.6% depending on flow Reynolds number. As R/D increases and the rib moves away from the stagnation point variation in both flow velocity and turbulence intensity increase, and this explains the effectiveness of placing the rib at a location near to stagnation point. For R/D=1.5, the percentage increase is between 3.6% and 10.6% whereas for R/D=2, there is an enhancement in heat transfer only for Re values of 20k and 30k, 6.4% and 15.3% respectively.

Effect of Turbulator Height - Flow Physics

This section presents the results of a simulation exercise on the effect of rib height (e) on normalized heat transfer coefficient averaged over a surface area $0 \leq R/D \leq 2.5$. The rib height was varied from 0.25 mm to 1.00 mm in increments of 0.25 mm to determine the optimum rib height that gave maximum heat transfer rate over the averaged area.

Fig. 5 shows local static pressure distribution for four heights of the rib roughening surface. For the stagnation point pressure, P, the figure shows that for Re=20k, an enhancement of local static pressure for all rib cases of approximately 27.5% when compared to the its value for the no rib case. This enhancement was reduced to only 2.3% when Re=40k. This may be due to the fact that the rib creates a pressure difference around itself that is sensitive to the flow in its vicinity Yuan & Piomelli [31].

This pressure difference then effects the main flow. As the flow moves forward to meet the rib, the local static pressure increases to a peak, which is larger the greater the rib height due to the increase in the impact area of the rib. This pressure peak is located where the flow hits the front of the rib as shown in the local static pressure contours of the same figure , for both Reynolds numbers. Beyond this point, a negative pressure occurs when the flow passes over the rib and a low pressure zone exists at the front edge of the horizontal surface of the rib. The absolute local value of this negative pressure increases with rib height and Reynolds number. In the case of 40k, increasing the rib height from e=0.25 mm to e=1.00 mm leads to an increase of the peak value of local maximum static pressure from 92 Pa to 187 Pa. Varying rib height influences local static pressure.

Fig. 6 shows the effect of varying Reynolds number and rib height on wall shear stress. For Re=20k, in the presence of a rib located at R/D = 1.5, all local wall shear values were higher than for the baseline by approximately 23% over the range R/D=0 to R/D≈1.2. However, for

Re=40k local wall shear values did not change from the baseline values until very close to the rib. The figure shows that when the flow reaches R/D≈1.2, the presence of the rib starts to affect the main flow by lowering the local wall shear values to almost zero, then there is a huge jump to a peak value at the face of the rib. The magnitude of this peak depends mainly on the rib height, and the peak is located on the top front edge of the rib where the flow impacts the rib, as shown in the figure. The figure also shows that e=0.25 mm, produces the greatest wall shear stress peak value with percentage increases of about 875% and 600% compared to the baseline case for Re=20k and 40k respectively. The figure shows that a rib of height of 1.00 mm produces the lowest peak value for both Reynolds numbers. For all radial locations ,R/D > 1.5, the local wall shear stress values are lower than the baseline case.

Effect of Turbulator Height - Heat Transfer Characteristic

Fig. 7 shows the effect of rib height on the local heat transfer coefficient, for R/D = 2, and Reynolds numbers 20k and 40k. It can be seen for the baseline with Re = 20k, the local heat transfer coefficient as a function of distance from the stagnation point can be represented as a smooth curve gradually decreasing as R increases. With a rib in place, the local heat transfer coefficient drops sharply to a minimum value immediately in front of the rib . The figure also shows that with increase in height of the rib the size of the flow vortices both in front of, and behind, the rib increase, and that means there will be an increase the heat transfer rate which confirms the work of other researchers such as [1, 32–34]. Generally, for all rib heights tested, there was an increase in the local heat transfer coefficient relative to the baseline case which shows itself as a peak close to the re-attachment point. The increase in local heat transfer increases with an increase in either or both of Reynolds number and rib height. For Re=20k, the rib height which gives maximum local heat transfer is e=0.50 mm, whereas for Re=40k, a rib height of e=0.25 mm gave the maximum heat transfer.

The normalized average heat transfer coefficient $\bar{h}/\bar{h}_o$ obtained when the rib was at a radial distance R/D=2 is shown in Fig. 8 for Reynolds numbers from 10k to 50k and rib height from 0.25 mm to 1.00 mm. For Re=10k, a rib located at R/D=2 an improvement of the average heat transfer rate over the area tested (0≤R/D≤2.5) was achieved between 6.6% to 10.1% using different rib height. Furthermore, for Re=20k, all rib heights gave an improvement in $\bar{h}/\bar{h}_o$ between 10% and 15.3% for e=0.25 mm and e=0.5 mm, respectively. Furthermore, As Reynolds number increases, the effect of rib height on the enhancement of heat transfer starts to show lower percentage values even lower than the baseline case for certain rib heights.

4. CONCLUSION

This paper has explored how controlling surface roughness can impact on heat transfer using a commercial simulation package [28]. First baseline conditions were established for a smooth, horizontal heated surface and then controlled surface roughness added in the form a continuous circular rib of square cross-section, concentric with an impinging jet of diameter D=13.5 mm normal to the surface. The radius of the rib (R) was varied from 1 to 1.5 to 2D, and the cross-section from 0.25 mm square to 1.00 mm square in steps of 0.25 mm. The Reynolds number of the impinging jet was in the range 10,000 to 50,000.

- In general, for low-range Reynolds numbers, Re=10,000 and 20,000, the variation of rib height and location reported maximum heat transfer enhancement between 5.4% to 12.9%. The maximum enhancement of heat transfer rate was achieved when the rib was located at R/D=2 for all tested Reynolds numbers and rib locations ≤ 0.75 mm.

- Rib location R/D=1 is located within the stagnation region which makes it less efficient when seeking an enhancement in heat transfer rate. While Rib height e= 1mm, has either no contribution in enhancement heat transfer or resulting *a* diminution between 10% to 30% in (AHTC) depending on Reynolds number and rib location.
- The flow failed to re-attach with the heated plate for rib height e=1mm, R/D=2 and Re=50,000.
- The higher the Reynolds number, the smaller the optimal rib height because of the combination between obstruction dimensions and flow patterns on heat transfer rate. For Re=30k, rib height = 1mm has no effect on heat transfer regardless of rib radial location. For higher Reynolds number values, Re=40,000 and 50,000, higher ribs can dramatically decrease heat transfer rate between 10% to 30% when compared to the baseline case.
- As the rib placed further in downstream location, the length of the vortices occur behind the rib increases between 6% to 57% depending On Reynolds numbers.
- The local static pressure at the stagnation point won't be substantially affected regardless of the rib location for lower and intermediate Reynolds numbers. As the rib location moves closer to the stagnation point, so the extent of the low-pressure region behind the rib increases, changing the distribution of the static pressure in this region.
- The rib has only a minor effect on wall shear from the stagnation point to a radial distance close to where rib is located. The magnitude of the peak wall shear stress decreases as the rib location moves downstream and as rib height increases.

The results present could have important practical applications regarding the design of, e.g., turbine blades and electronic devices for maximum heat removal.

For further research, the importance of the cross-sectional shape of the circular rib should be investigated. Combinations of ribs could also be considered with jet impingement angle and more general factors.

Acknowledgments

The authors acknowledge the valuable support and assistance provided

by Public Authority for Applied Education and Training (PAAET) in state of Kuwait.

Nomenclature

D	jet diameter (m)
H	jet-to-target distance (m)
R	radial distance (m)
y	flow direction coordinate (m)
e	rib height (m)
Re	Reynolds number (-)
T	temperature (k)
t	time (s)
y+	distance between the wall and the first node above it (-)
U_t	friction velocity (m/s)
y_w	vertical distance from the wall (m)
y	y-direction coordinates (m)
τ_w	wall shear stress (Pa)
h	local heat transfer coefficient (W $m^{-2}K^{-1}$)
$\bar{h}$	average heat transfer coefficient (AHTC) (W $m^{-2}K^{-1}$)
N_u	local Nusselt number (-)
$\overline{N_u}$	average Nusselt number (-)
P	static pressure (Pa)

Greek symbols

A	jet angle (°)
$\boldsymbol{\rho}$	density (kg/m^2)
μ	dynamic viscosity (m^2/s)
φ	convective wall heat flux density (W. m^2)

REFERENCES

[1] Xu, P., Sasmito, A. P., Qiu, S., Mujumdar, A. S., Xu, L., & Geng, L., 2016, Heat transfer and entropy generation in air jet impingement on a model rough surface, *International Communications in Heat and Mass Transfer*, *72*, 48–56. https://doi.org/10.1016/j.icheatmasstransfer.2016.01.007

[2] Gabour, L. a., Lienhard, J., H., 1994, Wall Roughness Effects on Stagnation-Point Heat Transfer Beneath an Impinging Liquid Jet, *Journal of Heat Transfer*, *116*(February), 81. https://doi.org/https://doi.org/10.1115/1.2910887

[3] Xing, Y., Spring, S., & Weigand, B., 2011, Experimental and numerical investigation of impingement heat transfer on a flat and micro-rib roughened plate with different crossflow schemes, *International Journal of Thermal Sciences*, *50*(7), 1293–1307. https://doi.org/https://doi.org/10.1016/j.ijthermalsci.2010.11.008

[4] Rao, Y., Chen, P., & Wan, C., 2016, Experimental and numerical investigation of impingement heat transfer on the surface with micro W-shaped ribs, *International Journal of Heat and Mass Transfer*, *93*, 683–694. https://doi.org/https://doi.org/10.1016/j.ijheatmasstransfer.2015.10.022

[5] Beitelmal, A., H., Saad, M., A., 2000, Effects of surface roughness on the average heat transfer of an impinging air jet, *International Communications in Heat and Mass Transfer*, *27*(1), 1–12. https://doi.org/https://doi.org/10.1016/S0735-1933(00)00079-8

[6] Ekkad, S., V., & Kontrovitz, D., 2002, Jet impingement heat transfer on dimpled target surfaces, *International Journal of Heat and Fluid Flow*, *23*(1), 22–28. https://doi.org/https://doi.org/10.1016/S0142-727X(01)00139-4

[7] Yilbas, B. S., Arif, A. F. M., & Abdul Aleem, B. J., 2010, Laser cutting of sharp edge: Thermal stress analysis, *Optics and Lasers in Engineering*, *48*(1), 10–19. https://doi.org/https://doi.org/10.1016/j.optlaseng.2009.03.006

[8] Sheikh-Ahmad, J., & Chipalkati, P., 2015, Effect of Cutting Edge Geometry on Thermal Stresses and Failure of Diamond Coated Tools, *Procedia Manufacturing*, *1*(Cvd), 663–674. https://doi.org/10.1016/j.promfg.2015.09.071

[9] Kim, W., S., Lee, S., Y., 2014, Behavior of a water drop impinging on heated porous surfaces, *Experimental Thermal and Fluid Science*, *55*, 62–70. https://doi.org/https://doi.org/10.1016/j.expthermflusci.2014.02.023

[10] Celik, N., 2011, Effects of the surface roughness on heat transfer of perpendicularly

impinging co-axial jet, *Heat and Mass Transfer/Waerme- und Stoffuebertragung*, *47*(10), 1209–1217. https://doi.org/DOI 10.1007/s00231-011-0785-9

[11] Xing,Y., Weigand, B., 2010, Experimental investigation of impingement heat transfer on a flat and dimpled plate with different crossflow schemes, *International Journal of Heat and Mass Transfer*, *53*(19–20), 3874–3886. https://doi.org/https://doi.org/10.1016/j.ijheatmasstransfer.2010.05.006

[12] Nadda, R., Kumar, A., & Maithani, R., 2017, Developing heat transfer and friction loss in an impingement jets solar air heater with multiple arc protrusion obstacles, *Solar Energy*, *158*(June), 117–131. https://doi.org/10.1016/j.solener.2017.09.042

[13] Wang, S., Du, W., Luo, L., Qiu, D., Zhang, X., & Li, S., 2018, Flow structure and heat transfer characteristics of a dimpled wedge channel with a bleed hole in dimple at different orientations and locations, *International Journal of Heat and Mass Transfer*, *117*, 1216–1230. https://doi.org/10.1016/j.ijheatmasstransfer.2017.10.087

[14] Alhajeri, H. M., Almutairi, A., Alenezi, A. H., & Gamil, A. A. A., 2019, Numerical investigation on heat transfer performance and flow characteristics in a roughened vortex chamber, *Applied Thermal Engineering*, *153*(January), 58–68. https://doi.org/10.1016/j.applthermaleng.2019.02.071

[15] Attalla, M., Abdel Samee, A. A., & N. Salem, N., 2020, Experimental investigation of heat transfer of impinging jet on a roughened plate by a micro cubic shape, *Experimental Heat Transfer*, *33*(3), 210–225. https://doi.org/10.1080/08916152.2019.1614113

[16] Wang, G., Qian, N., & Ding, G., 2019, Heat transfer enhancement in microchannel heat sink with bidirectional rib, *International Journal of Heat and Mass Transfer*, *136*, 597–609. https://doi.org/10.1016/j.ijheatmasstransfer.2019.02.018

[17] Tullius, J. F., Tullius, T. K., & Bayazitoglu, Y., 2012, Optimization of short micro pin fins in minichannels, *International Journal of Heat and Mass Transfer*, *55*(15–16), 3921–3932. https://doi.org/10.1016/j.ijheatmasstransfer.2012.03.022

[18] Prajapati, Y. K., 2019, Influence of fin height on heat transfer and fluid flow characteristics of rectangular microchannel heat sink, *International Journal of Heat and Mass Transfer*, *137*, 1041–1052. https://doi.org/10.1016/j.ijheatmasstransfer.2019.04.012

[19] Kewalramani, G. V., Hedau, G., Saha, S. K., & Agrawal, A., 2019, Study of laminar single phase frictional factor and Nusselt number in In-line micro pin-fin heat sink for electronic cooling applications, *International Journal of Heat and Mass Transfer*, *138*, 796–808. https://doi.org/10.1016/j.ijheatmasstransfer.2019.04.118

[20] Choudhary, V., Kumar, M., & Patil, A. K., 2019, Experimental investigation of enhanced performance of pin fin heat sink with wings, *Applied Thermal Engineering*, *155*(November 2018), 546–562. https://doi.org/10.1016/j.applthermaleng.2019.03.139

[21] Yang, D., Jin, Z., Wang, Y., Ding, G., & Wang, G., 2017, Heat removal capacity of laminar coolant flow in a micro channel heat sink with different pin fins, *International Journal of Heat and Mass Transfer*, *113*, 366–372. https://doi.org/10.1016/j.ijheatmasstransfer.2017.05.106

[22] Wang, Y., Zhu, K., Cui, Z., & Wei, J., 2019, Effects of the location of the inlet and outlet on heat transfer performance in pin fin CPU heat sink, *Applied Thermal Engineering*, *151*(May 2018), 506–513. https://doi.org/10.1016/j.applthermaleng.2019.02.030

[23] Wang, G., Chen, T., Tian, M., & Ding, G., 2020, Fluid and heat transfer characteristics of microchannel heat sink with truncated rib on sidewall, *International Journal of Heat and Mass Transfer*, *148*, 119142. https://doi.org/10.1016/j.ijheatmasstransfer.2019.119142

[24] Ravanji, A., & Zargarabadi, M. R., 2020, Effects of elliptical pin-fins on heat transfer characteristics of a single impinging jet on a concave surface, *International Journal of Heat and Mass Transfer*, *152*, 119532. https://doi.org/10.1016/j.ijheatmasstransfer.2020.119532

[25] Hadipour, A., Rajabi Zargarabadi, M., & Dehghan, M., 2020, Effect of micro-pin characteristics on flow and heat transfer by a circular jet impinging to the flat surface, *Journal of Thermal Analysis and Calorimetry*, *140*(3), 943–951. https://doi.org/10.1007/s10973-019-09232-2

[26] O'Donovan, T., S., Murray, B., D., 2007, Jet impingement heat transfer - Part I: Mean and root-mean-square heat transfer and velocity distributions, *International Journal of Heat and Mass Transfer*, *50*(17–18), 3291–3301. https://doi.org/10.1016/j.ijheatmasstransfer.2007.01.044

[27] Alimohammadi, S., Murray, D. B., & Persoons, T., 2014, Experimental validation of a computational fluid dynamics methodology for transitional flow heat transfer characteristics of a steady impinging jet, *Journal of Heat Transfer*, *136*(9), 1–10. https://doi.org/10.1115/1.4027840

[28] ANSYS Fluent Tutorial Guide 18, 2018, ANSYS Fluent Tutorial Guide 18, *ANSYS Fluent Tutorial Guide 18*, *15317*(April), 724–746.

[29] Baghel, K., Sridharan, A., & Murallidharan, J. S., 2019, Numerical study of free surface jet impingement on orthogonal surface, *International Journal of Multiphase Flow*, *113*, 89–106. https://doi.org/10.1016/j.ijmultiphaseflow.2019.01.001

[30] Sagot, B., Antonini, G., Christgen, A., & Buron, F., 2008, Jet impingement heat transfer on a flat plate at a constant wall temperature, *International Journal of Thermal Sciences*, *47*(12), 1610–1619. https://doi.org/10.1016/j.ijthermalsci.2007.10.020

[31] Yuan, J., & Piomelli, U., 2014, Estimation and prediction of the roughness function on realistic surfaces, *Journal of Turbulence*, (June 2015), 1–6. https://doi.org/10.1080/14685248.2014.907904

[32] Katti, V., & Prabhu, S., V., 2008, Heat transfer enhancement on a flat surface with axisymmetric detached ribs by normal impingement of circular air jet, *International Journal of Heat and Fluid Flow*, *29*(5), 1279–1294. https://doi.org/https://doi.org/10.1016/j.ijheatfluidflow.2008.05.003

[33] Gau, C., & Lee, I., C., 2000, Flow and impingement cooling heat transfer along triangular rib-roughened walls, *International Journal of Heat and Mass Transfer*, *35*(11), 3009–3020. https://doi.org/10.1016/S0017-9310(00)00064-8

[34] Zhou, J., W., Wang, Y., G., Middelberg, G., & Herwig, H., 2009, Unsteady jet impingement: Heat transfer on smooth and non-smooth surfaces, *International Communications in Heat and Mass Transfer*, *36*(2), 103–110. https://doi.org/https://doi.org/10.1016/j.icheatmasstransfer.2008.10.020

Figure Caption List

Fig. 1 Computational domain and grid topology.

Fig. 2 Model validation for H/D=6, Re=10,000 and α=90°, (a) Grid dependency, (b) Numerical model and (c) Average Nusselt number validation

Fig. 3 Local static pressure distribution in radial direction for variable Re values.

Fig. 4 Local wall shear stress distribution in radial direction for different Re.

Fig. 5 Average Heat transfer coefficient distribution in radial direction for different Re, average values over $0 \leq R/D \leq 2.5$

Fig. 6 Velocity contours of rib height e=1 mm, Re=50k and different rib locations (R/D)

Fig. 7 local static pressure for e=0.50 mm, with three values of Re and radial locations, R/D.

Fig. 8 Wall shear distribution and velocity streamlines in the radial direction for e=0.50 mm, Re=30,000 for (a) R/D=1, (b)R/D=1.5 and (c) R/D=2.

Fig. 9 Contour and Local heat transfer distribution for e=0.50 mm, R/D=1,1.5 and 2 and Re=10k,30k and 50k.

Fig. 5 Normalized average heat transfer coefficient for e=0.50 mm, different Reynolds numbers and different values of R/D.

Fig. 6 Contour and local static pressure distribution and contours for Re=20,000 and 40,000, and different rib heights (e).

Fig. 7 Contour and local wall shear distribution and contours for Re=20,000 and 40,000, and three rib heights.

Fig. 8 Effect of rib height on local Nusselt number for Re= 20k and 40k, H/D=6.

Fig. 14 Normalized average heat transfer coefficient for different rib sizes, Reynolds numbers and rib locations.

Figures

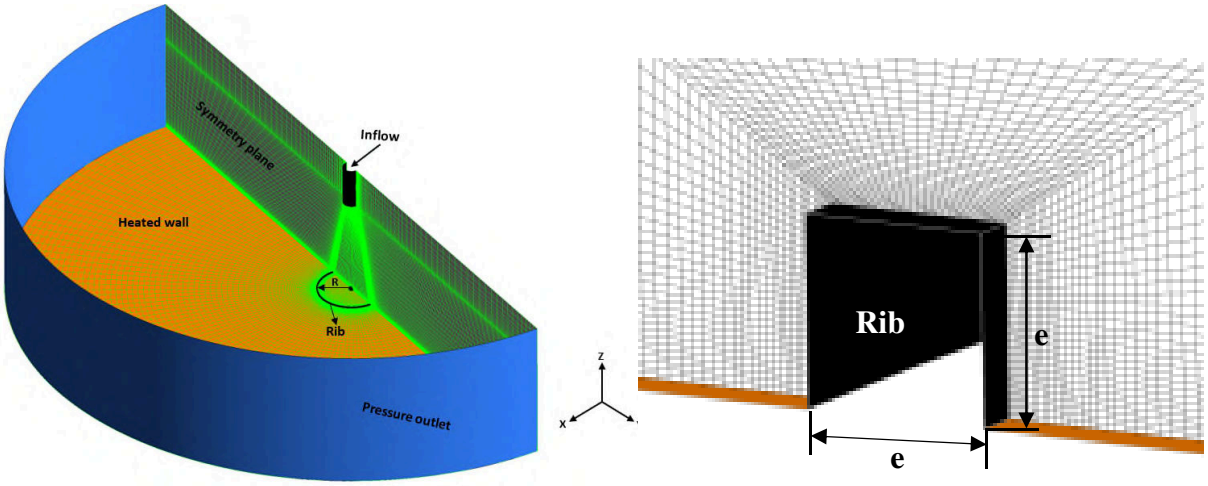
Symmetry plane
Inflow
Heated wall
R
Rib
Pressure outlet
Z
X
Rib
e
e

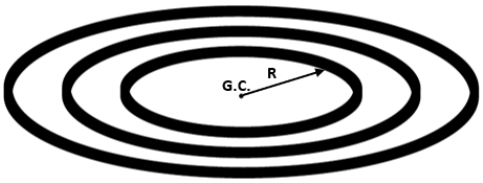

Fig. 1 Computational domain and grid topology

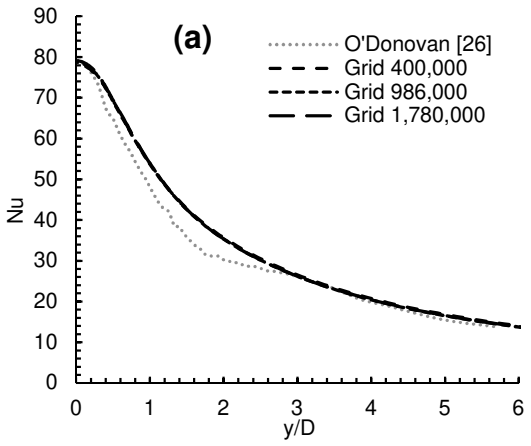

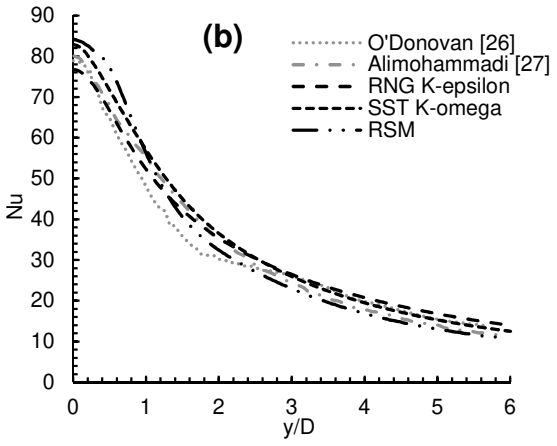

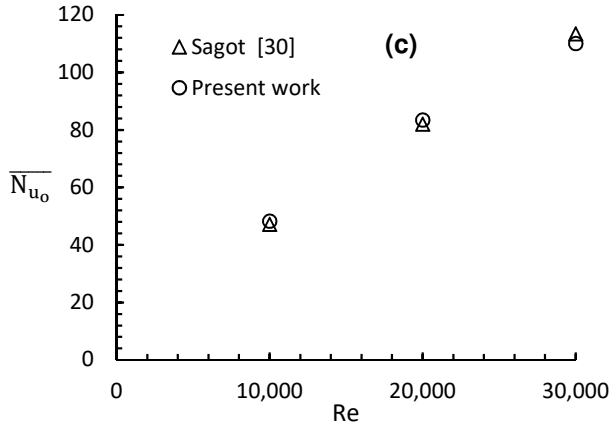

Fig. 2 Model validation for H/D=6, Re=10,000 and α=90°, (a) Grid dependency, (b) Numerical model and (c) Average Nusselt number validation

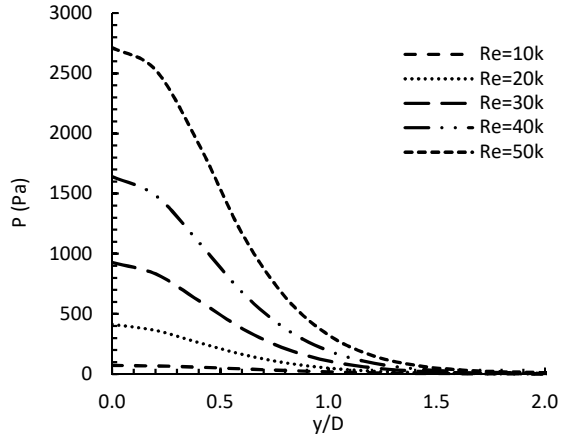

Fig.3 Local static pressure distribution in radial direction for variable Re values

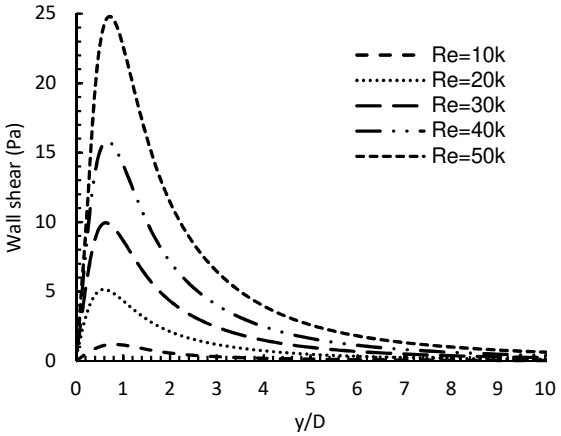

Fig. 4 Local wall shear stress distribution in radial direction for different Re

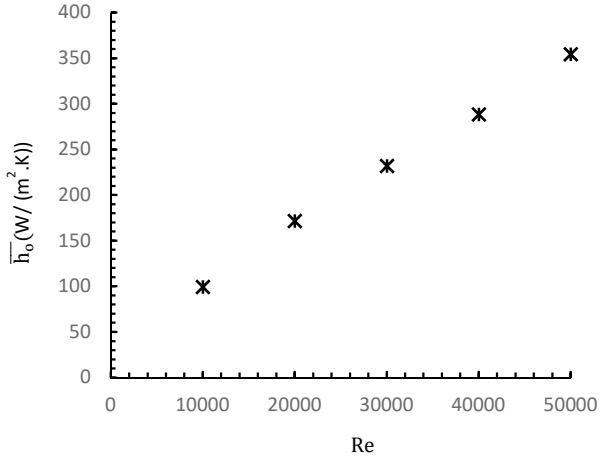

Fig. 5 Average Heat transfer coefficient distribution in radial direction for different Re, average values over 0 ≤ R/D ≤ 2.5

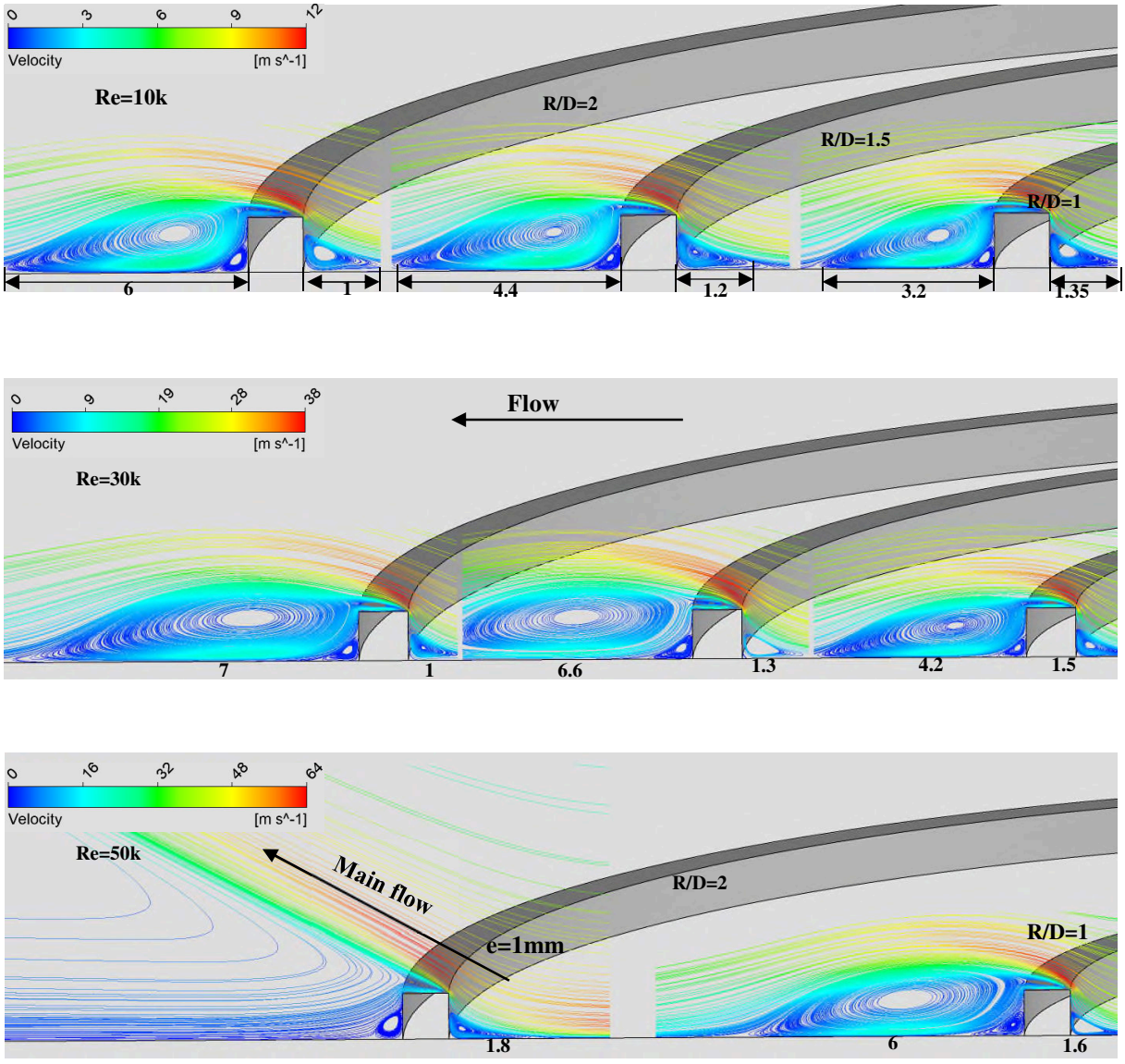

(All dimensions in mm)

Fig. 6 Velocity contours of rib height e=0.5 mm, Re=50k and different rib locations (R/D)

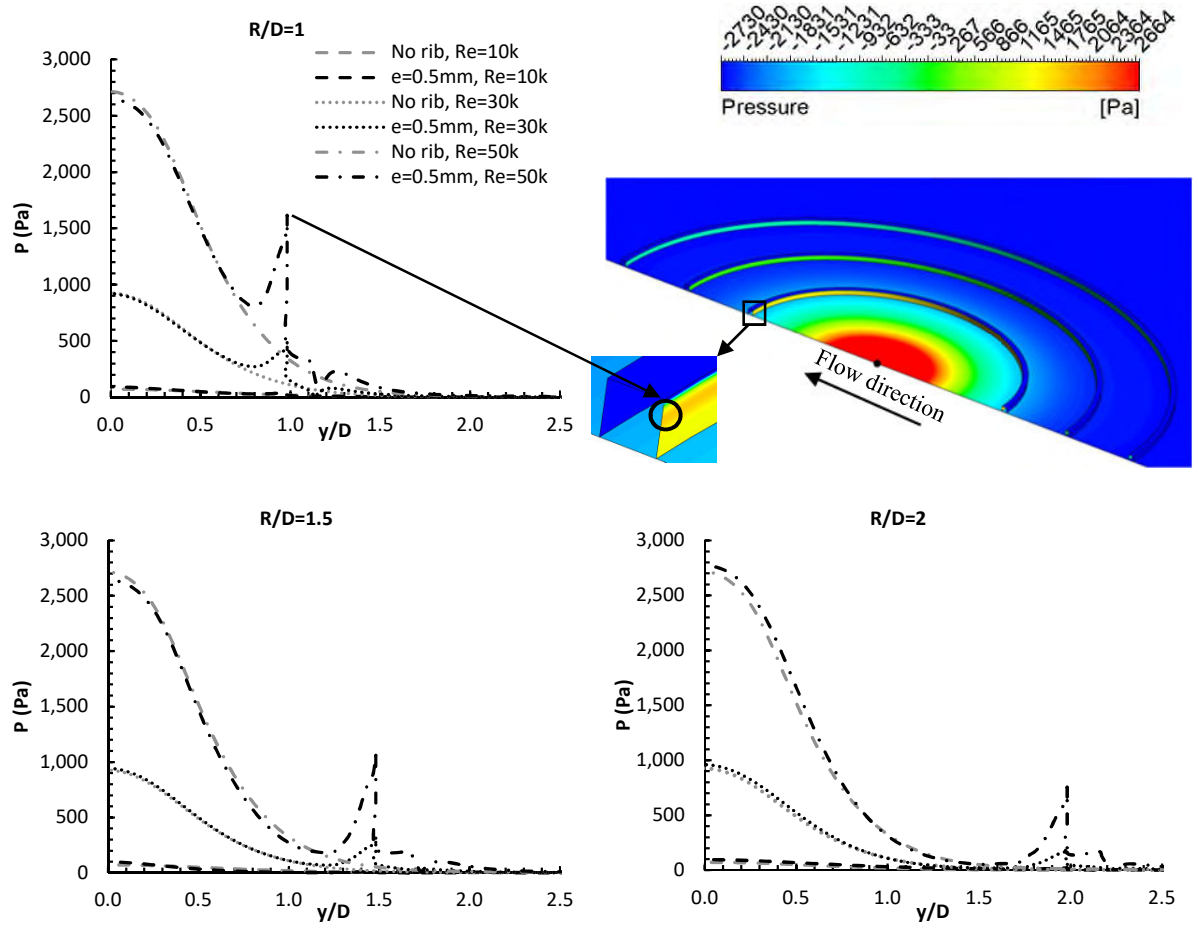

Fig. 7 Local static pressure for e=0.50 mm, with three values of Re and radial locations, R/D

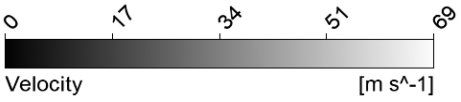

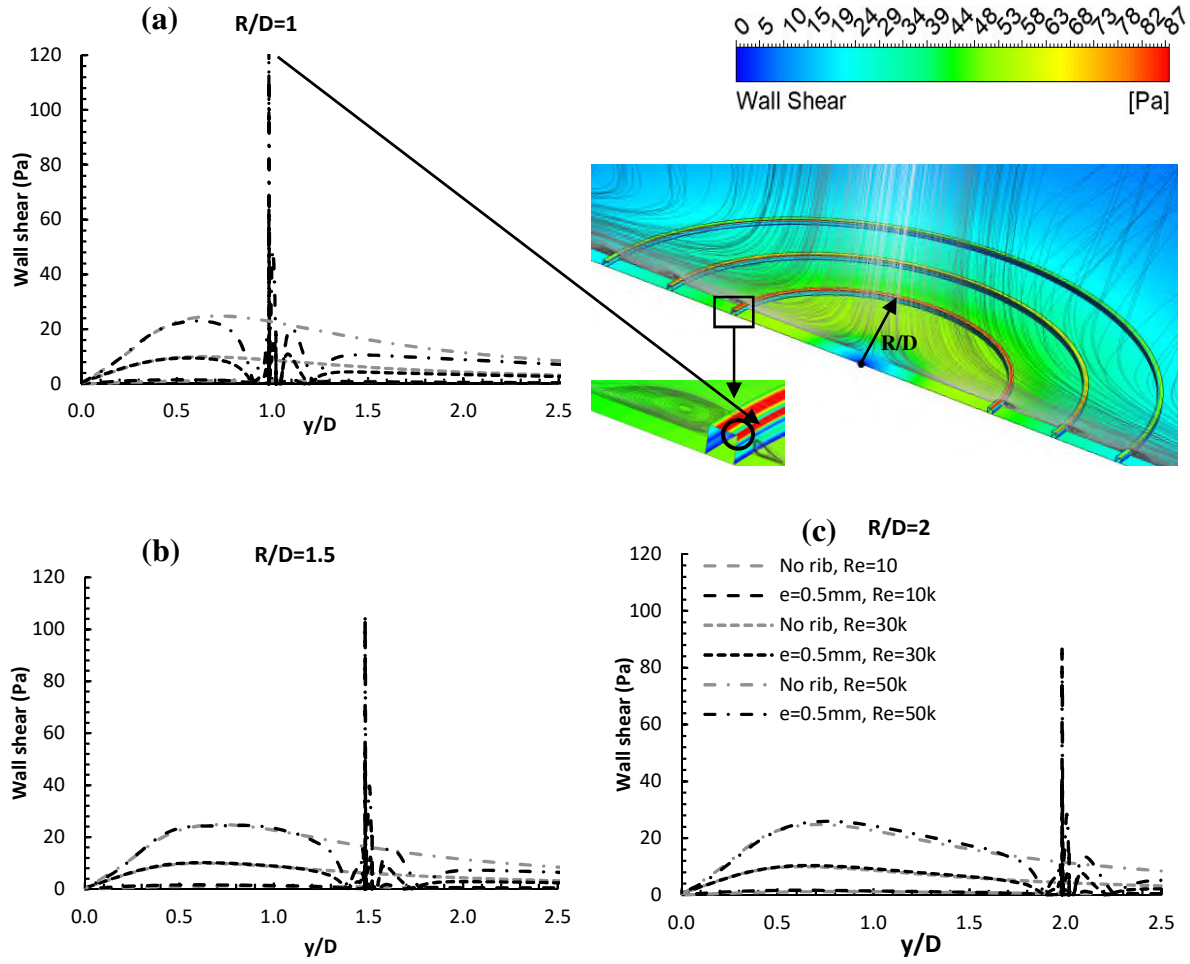

Fig. 8 Wall shear distribution and velocity streamlines in the radial direction for e=0.50 mm, Re=30,000 for (a) R/D=1, (b)R/D=1.5 and (c) R/D=2

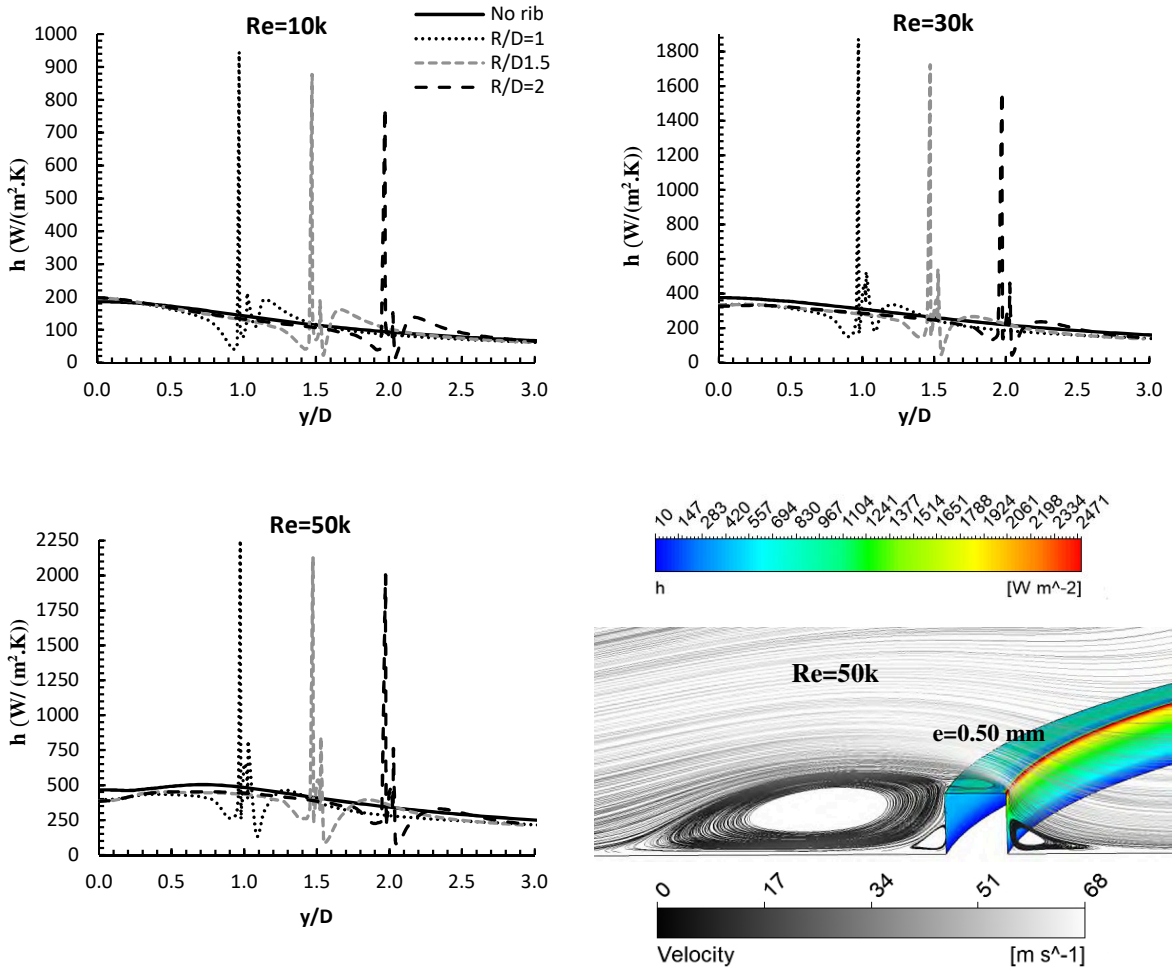

Fig. 9 Contour and Local heat transfer distribution for e=0.50 mm, R/D=1,1.5 and 2 and Re=10k,30k and 50k

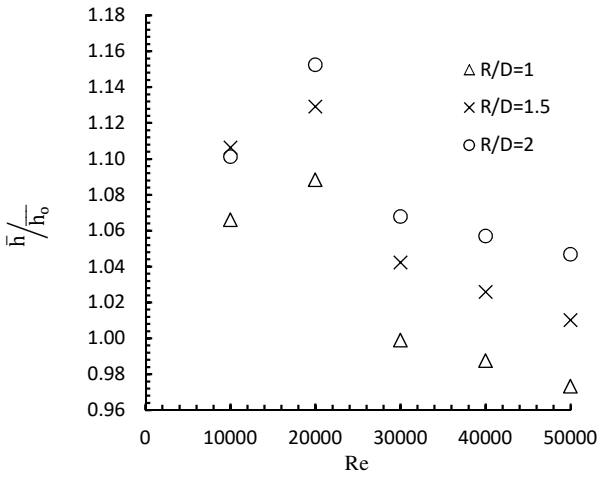

Fig. 10 Normalized average heat transfer coefficient for e=0.50 mm, different Reynolds numbers and different values of R/D

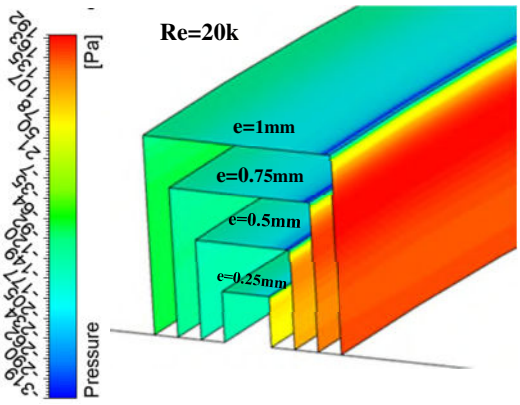

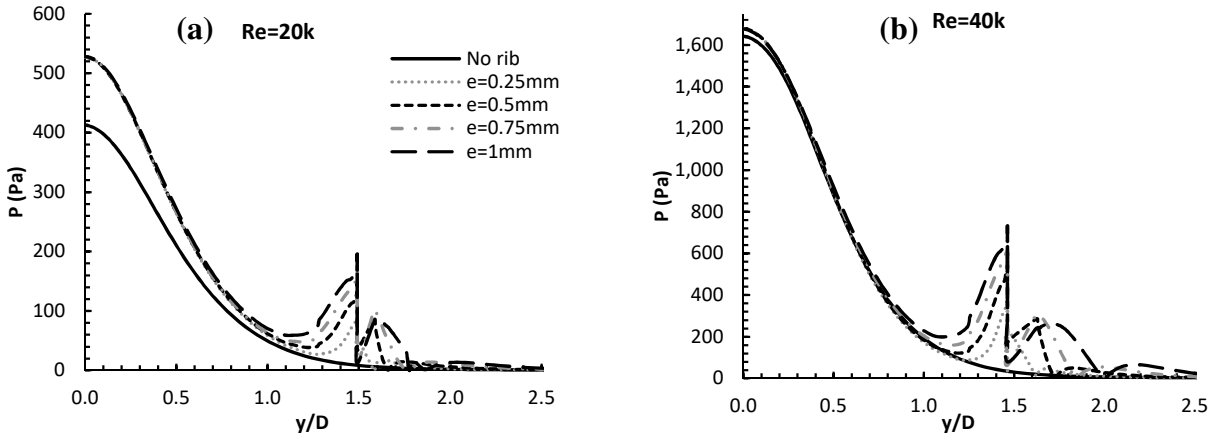

Fig. 11 Contour and local static pressure distribution and contours for Re=20,000 and 40,000, and different rib heights (e)

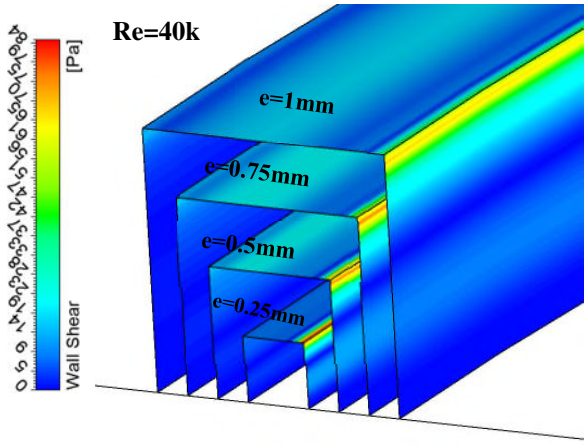

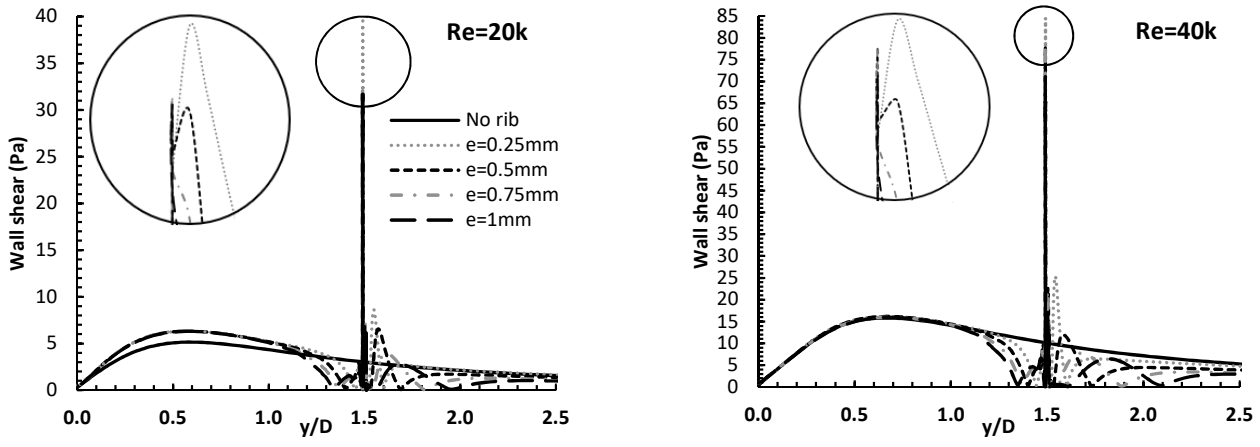

Fig. 12 Contour and local wall shear distribution and contours for Re=20,000 and 40,000, and three rib heights

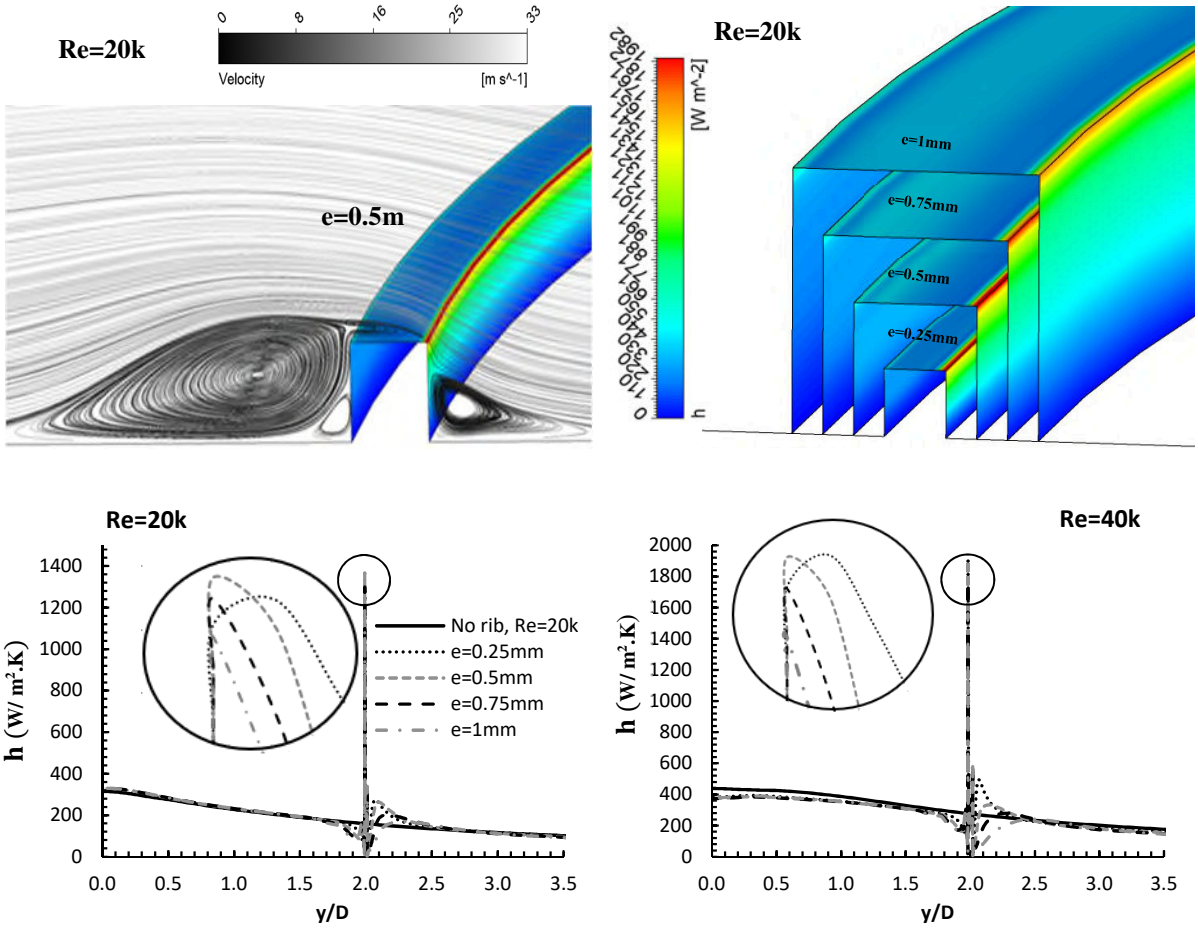

Fig. 13 Effect of rib height on local Nusselt number for Re= 20k and 40k, H/D=6

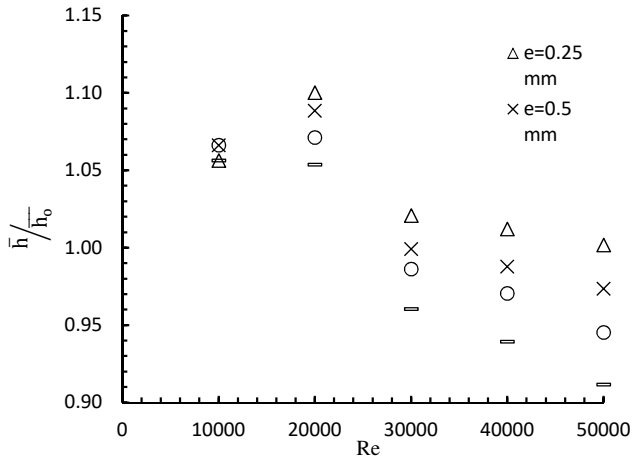

Fig. 14 Normalized average heat transfer coefficient for different rib sizes, Reynolds numbers and rib location, R/D=1

Numerical investigation on turbulence statistics and heat transfer of a circular jet impinging on a roughened flat plate

Alenezi, Abdulrahman H.

2020-10-13

Alenezi A, Almutairi A, Alhajeri H, et al., (2022) Numerical investigation on turbulence statistics and heat transfer of a circular jet impinging on a roughened flat plate. Journal of Thermal Science and Engineering Applications, Volume 13, Issue 4, August 2022, Article number 041010; Paper number TSEA-20-1428

https://doi.org/10.1115/1.4048757